

## S1. Sample preparation

Symmetric-type diamond-anvil cells (DAC) were used to perform experiments at high  $P$ - $T$  conditions. A rhenium gasket was indented by two diamond-anvils to a thickness of  $\sim 20 \mu\text{m}$  and a diameter of 200 or 300  $\mu\text{m}$ . Using a laser drilling system in Arizona State University (ASU), a 130–180  $\mu\text{m}$  diameter hole, a sample chamber, was made at the center of the indentation. The drilled rhenium gasket was coated with gold to prevent the H diffusion into the gasket material. MgO (Alfa Aesar, 99.95% purity) powder was dried at 388 K for 24 hours in an oven and then mixed with 20 wt% Fe metal (Sigma Aldrich, 99.9% purity) in a mortar. The mixed powder was compressed to a  $\sim 10\text{-}\mu\text{m}$  thin foil. To prevent contact with the diamond anvils and make a space for  $\text{H}_2$ , the foil was propped by 2–3  $\mu\text{m}$  MgO grains on the culets of both diamond anvils. Pure  $\text{H}_2$  gas (Matheson Tri-Gas, Inc.) compressed to 1300 bar was loaded in the sample chamber together with the foil using a gas loading system at ASU (Sanchez Technologies). After closing the DAC, the pressure of the sample chamber measured from ruby chips (54) was  $\sim 1$  GPa. Before synchrotron measurements, the samples were compressed to target pressures between 5 and 25 GPa.

## S14 S2. Laser-heated diamond-anvil cell experiments

Experiments were conducted at beamline 13-IDD of the GeoSoilEnviroCARS (GSECARS) sector at the Advanced Photon Source (APS). A double-sided laser-heating setup at the beamline focuses infrared laser beams on both sides of the sample. The laser beams were aligned coaxially with the X-ray beam. The diameter of the heated area was  $\sim 20 \mu\text{m}$  (18). In previous experimental studies using pure  $\text{H}_2$  medium (for examples, (51)), it was found that a continuous heating for sample in an  $\text{H}_2$  medium could shatter diamond anvils within a few second. The reason is because  $\text{H}_2$  molecules are small enough to diffuse into diamond anvils at high pressure and such a behavior is further promoted by heating. To avoid the diamond embrittlement issue by H diffused into the diamond anvils during continuous heating to the melting temperature of MgO, we conducted pulsed laser heating (19–21). This heating method allowed us to reach above 4000 K for the sample in a diamond-anvil cell. Because pulse-heating tends to reduce the mechanical damage of the sample foil by the convection of H fluid at high temperatures, it can preserve a heated sample better. However, the percentage of the samples recovered for chemical analysis is still as low as 30–50% because of the severe fracturing of the sample foils by intense reaction with an H fluid (Fig. S2a). During heating, thermal radiation spectra were measured for the both side of the sample.

Temperature was estimated by fitting the measured spectra to the gray-body radiation equation for 680–840 nm range. Temperature uncertainty is estimated considering 1) the uncertainties from the spectral fitting, 2) temperature differences between the two sides of the sample, and 3) temperature fluctuations during pulsed laser heating (Table S1). We estimated pressures at high temperatures using the measured volume of MgO combined with its thermal equation of state (23). Estimated  $1\sigma$  uncertainty for pressure is  $\pm 10\%$ . A monochromatic X-ray beam (a wavelength of 0.3344 Å) was focused to  $3 \times 2 \mu\text{m}^2$  in size.

A pixel array detector (Pilatus 3X CdTe 1M) was used for measuring X-ray diffraction (XRD) images. Diffraction images were measured at in situ high  $P$ - $T$  conditions as well as after heating at 300 K.

Additional XRD measurements were also conducted at beamline 13-BMD of GSECARS with a monochromatic X-ray beam (a wavelength of 0.3344 Å) focused to  $4 \times 9 \mu\text{m}^2$ . The same type of detector was used. XRD data for  $\text{LaB}_6$  standard were measured to correct for the detector tilt and to obtain sample-to-detector distance,  $\sim 200$  mm. 2D XRD images were converted to one-dimensional XRD patterns using the Dioptas software (55). Peak identification and unit-cell fitting were conducted using the PeakPo software package (56).

## S43 S3. Raman spectroscopy

Raman spectroscopy measurements were conducted at 200–4500  $\text{cm}^{-1}$  using a system at GSECARS (24). A 532-nm laser used as an excitation source. The laser power was 0.05 or 0.1 Watts, and the grating was

S46 1200 grooves/mm in the spectrograph (Princeton Instruments Acton Series 2500; a focal length of 500 mm).  
S47  $8 \times 8 \mu\text{m}^2$  areas at the heated areas were mapped with a  $4\text{-}\mu\text{m}$  step (i.e., 25 spectra per single map). Each  
S48 spectrum was measured for 10 seconds. Unheated areas and hydrogen-only areas in the sample chamber  
S49 were also measured to compare with the spectra from the heated areas. Similar measurements were also  
S50 conducted using a Raman system at ASU.

## S51 S4. Chemical analysis

S52 The recovered samples were analyzed in electron microscopes for the chemical composition and the  
S53 structure in the heated areas. For scanning electron microscopy (SEM) analysis and energy-dispersive X-ray  
S54 spectroscopy (EDS), we milled the recovered sample using a focused ion beam (FIB) instrument (Helios  
S55 5 UX, Thermo Fisher Scientific Inc.) at Arizona State University (ASU). For SEM imaging and EDS,  
S56 we milled the heated areas for cross sections using the focused  $\text{Ga}^+$  ion beam with 30 keV and 9 nA for  
S57 initial milling, and 30 keV and 2.6 nA for the final milling. SEM images were obtained at 10 keV or 15 keV.  
S58 Two-dimensional elemental distribution maps were measured at 10 keV using EDS (Xflash 6|30 detector,  
S59 Bruker co.) for Mg, Fe, and O. For transmission electron microscopy (TEM) analysis and EDS, thin sections  
S60 ( $\sim 6 \times 6 \mu\text{m}^2$ ) were extracted from the heated areas using the  $\text{Ga}^+$  ion beam with 30 keV and 0.26 nA in the  
S61 same FIB instrument at ASU. Due to the cracks and fractures in the heated areas, we could not avoid  
S62 some irregularities during thinning (e.g., vertical streaks in Fig. 4a). The thin specimen was moved on a  
S63 copper grid for further thinning to  $\sim 100$  nm thickness at 2 keV and 44 pA. In a ARM-200F (JEOL co. at  
S64 ASU) STEM, the samples were imaged with an acceleration voltage of 80 keV. TEM images were obtained  
S65 under a high-angle annular dark field scanning transmission-electron microscope (HAADF-STEM) mode.  
S66 Chemical data were acquired using energy dispersive X-ray spectroscopy for 20–30 seconds. Elemental  
S67 analysis was conducted for Mg, Fe, and O.

## S68 S5. Pressures at the interface between atmosphere and magma in sub-Neptunes

S69 For sub-Neptune exoplanets with a 2%  $\text{H}_2$  atmosphere and an Earth-like interior composition, the planet's  
S70 mass can be calculated for the cases of  $P(\text{AMB}) = 15, 20,$  and  $25$  GPa using equations 9–11 and 21–22 in  
S71 (8). From the mass and  $M = (1.74 \pm 0.38)R^{(1.58 \pm 0.10)}$ , suggested by (45) for a mass range of  $5\text{--}25M(E)$ ,  
S72 radius can be calculated. The planet's radii for  $P(\text{AMB}) = 15, 20,$  and  $25$  GPa are  $2.52, 3.03,$  and  $3.48R(E)$ ,  
S73 respectively (Fig. 5).

S74 A slightly different method can be used, but with essentially the same results within the uncertainties.  
S75 The radius cliff is observed at  $\sim 3R(E)$  (13, 14, 44). To calculate the pressure at the atmosphere-magma  
S76 boundary of sub-Neptunes using equation 22 in (8),  $\text{H}_2$  percentage and the mass of planet are required. The  
S77 mass-radius relation of sub-Neptunes with a 2%  $\text{H}_2$  atmosphere (equilibrium temperature ( $T_E$ ) of 700 K)  
S78 and Earth-like core exists at  $3.0 \pm 0.2 R(E)$  between  $5M(E)$  and  $15M(E)$  (8). We estimated the pressure  
S79 range for the atmosphere-magma boundary shown in Fig. 1 from three chosen planets: Kepler-1808b  
S80 ( $T_E = 601$  K;  $9.41M(E)$ ;  $3.03R(E)$ ), Kepler-1717b ( $T_E = 780$  K;  $9.22M(E)$ ;  $2.99R(E)$ ) and TOI-220b  
S81 ( $T_E = 806$  K;  $13.6M(E)$ ;  $3.02R(E)$ ) assuming a 2%  $\text{H}_2$  atmosphere.

S82 54. Mao HK, Xu J, Bell PM (1986) Calibration of the ruby pressure gauge to 800 kbar under quasi-hydrostatic conditions. *J. Geophys. Res.* 91(B5):4673.

S83 55. Prescher C, Prakapenka VB (2015) *DIOPYAS*: A program for reduction of two-dimensional X-ray diffraction data and data exploration. *High Pressure Research* 35(3):223–230.

S84 56. S.-H. Dan Shim (2017) SHDShim/peakpo-v7: Improvement in UI (Zenodo).

S85 57. Kato C, et al. (2020) Stability of fcc phase FeH to 137 GPa. *American Mineralogist* 105(6):917–921.

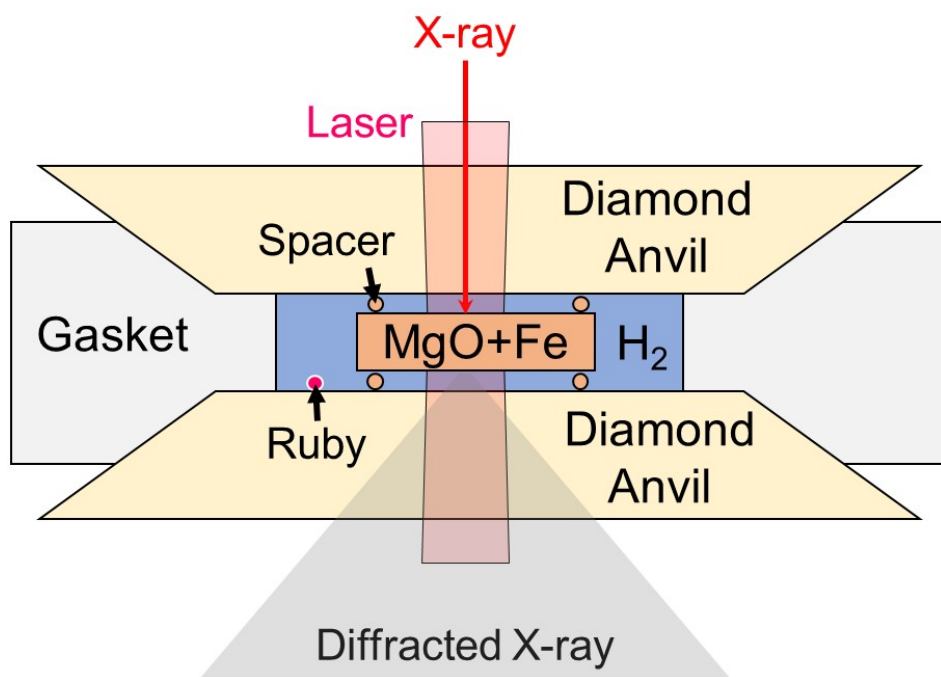


**Fig. S1.** The sample setup in a diamond-anvil cell used in this study.

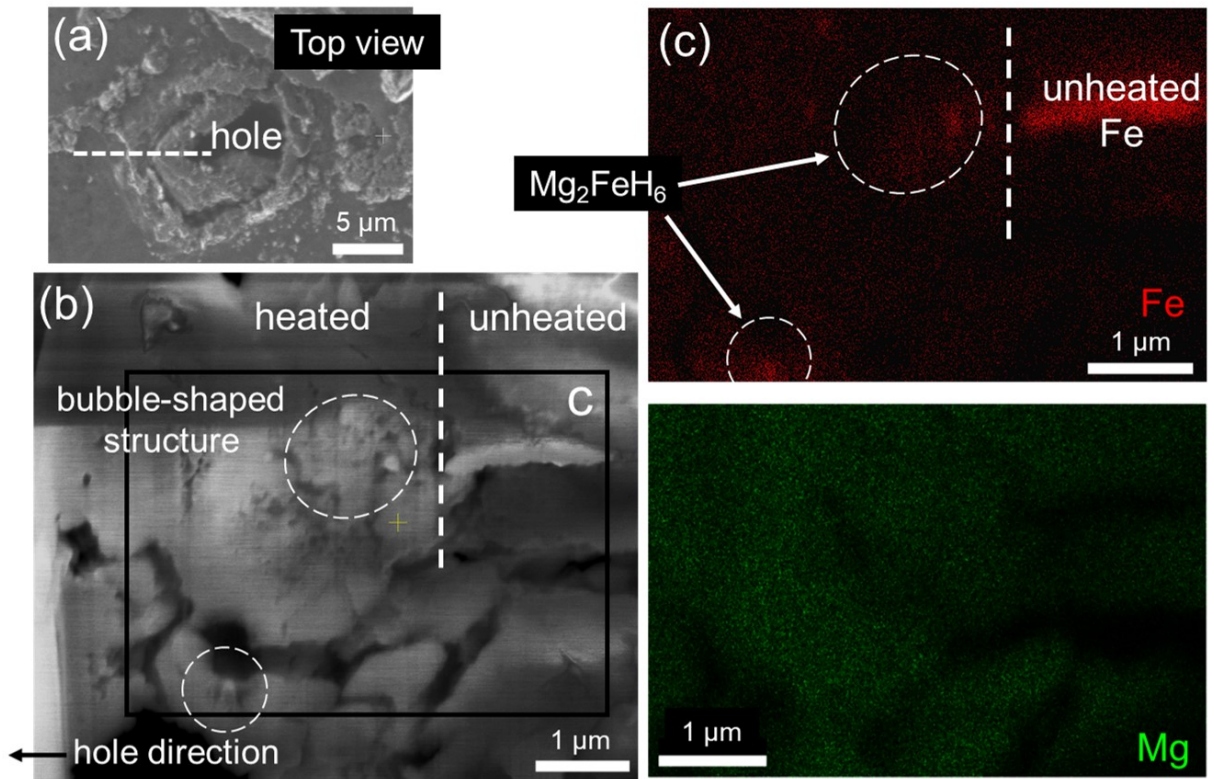


**Fig. S2.** Scanning electron microscopy (SEM) images (a and b) and the energy-dispersive spectroscopy (EDS) maps (c) of the heated area in the samples recovered from run #31-005 (12.5 GPa and 4770 K). (a) A top view of the heated area. The hole at the center is from the transport of the melt away from the spot by an H fluid during heating. A white dashed line shows the location of the cross section in b. (b) An SEM image showing small cavities in the heated area (the left side of a dashed line). (c) Elemental distribution maps for Fe and Mg. The two white circles with a weaker Fe signal than the Fe metal in the unheated area and a weaker Mg signal than the surrounding MgO area can be assigned to  $\text{Mg}_2\text{FeH}_6$ , which contains both Mg and Fe, unlike MgO. The circled areas contain small cavities as shown in (b). According to Eq. 1,  $\text{Mg}_2\text{FeH}_6$  and  $\text{H}_2\text{O}$  should crystallize together upon temperature quench at high pressure. When the DAC was opened,  $\text{H}_2\text{O}$  becomes a liquid and is eventually evaporated, leaving the small cavities. Therefore, both the chemical map and the texture can support the interpretation for  $\text{Mg}_2\text{FeH}_6$ .

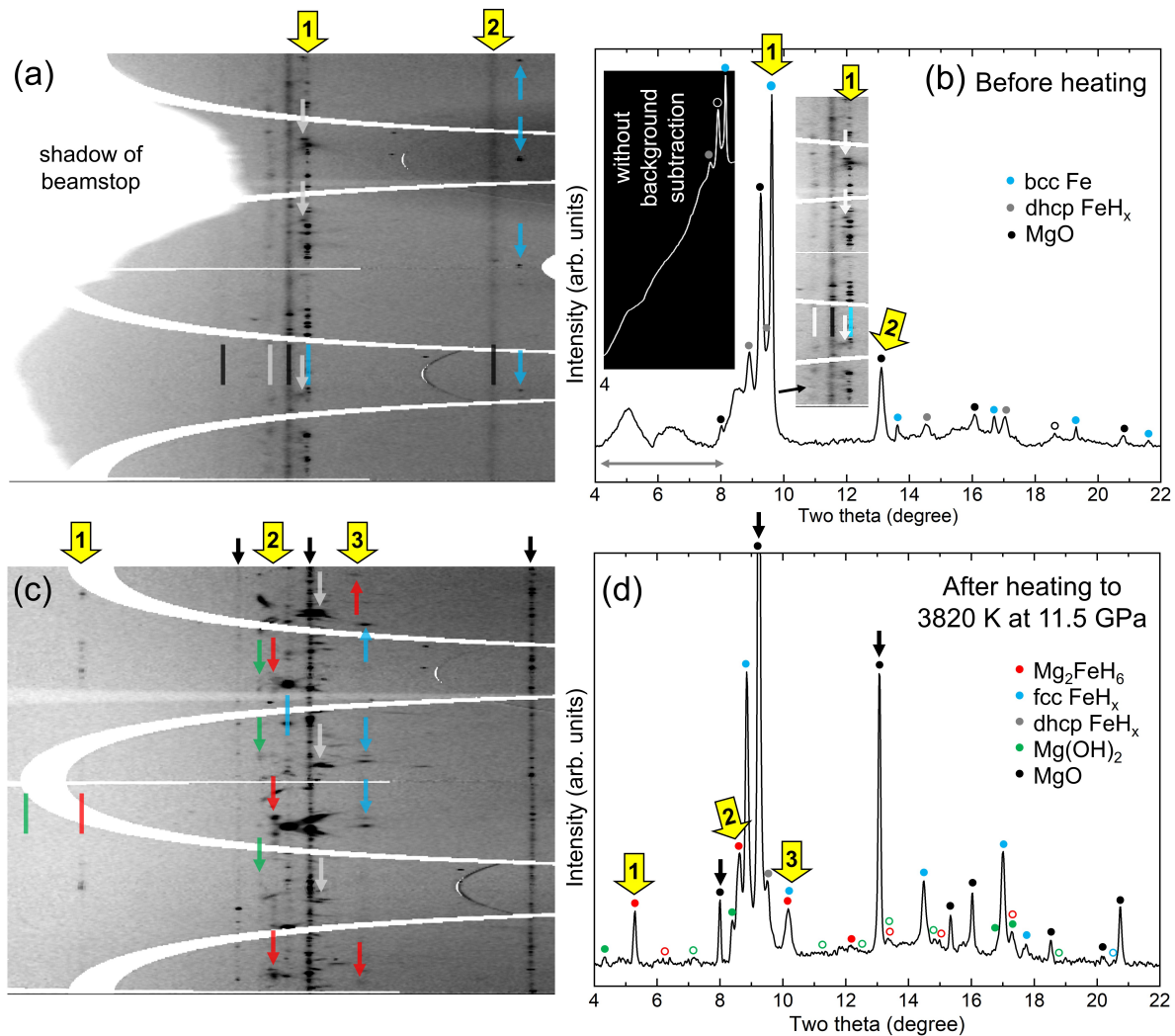


**Fig. S3.** X-ray diffraction images (unrolled) and patterns measured (a,b) before heating, and (b,c,d) after heating to 3820 K at 11.5 GPa from run #31-003. The circles above the peaks mark the peak positions for the observed phases calculated from their crystal structures and equations of state. For the peaks which are predicted but not observed, open circles are used. The [yellow arrows](#) [insets](#) in the [unrolled diffraction image \(c\)](#) and the [diffraction pattern \(d\)](#) [of \(b\)](#) [show part of the unrolled diffraction images](#) [indicate for](#) the major peaks of  $\text{Mg}_2\text{FeH}_6$ .



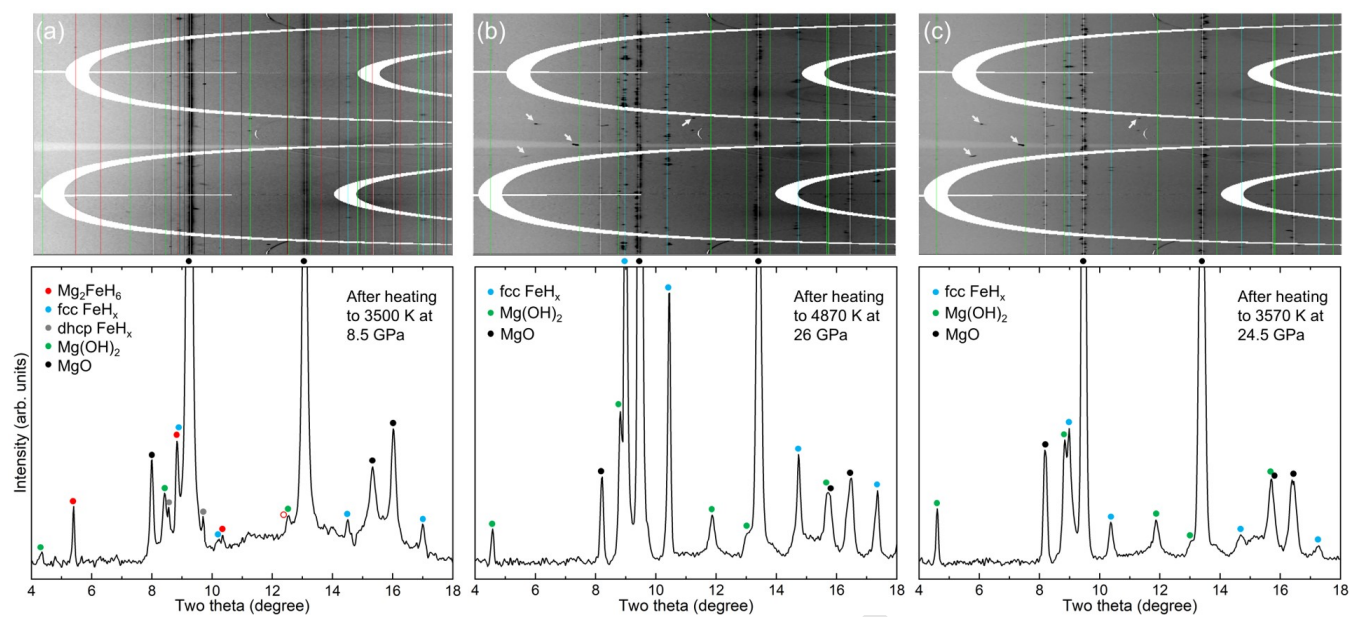


**Fig. S4.** X-ray diffraction images (unrolled) and patterns measured after heating to (a) 3500 K at 8.5 GPa, (b) 4870 K at 26 GPa, and (c) 3570 K at 24.5 GPa. The circles above the peaks mark the peak positions for the observed phases calculated from their crystal structures and equations of state. The open circles indicate predicted positions for the diffraction peaks of the observed phases, but the peaks were not observed at the positions. The white arrows in the 2D images indicate defects in the detector. The diffraction pattern in (a) was in different beamtime and therefore the detector defects were not seen there. (b) and (c) were measured during the same beamtime.

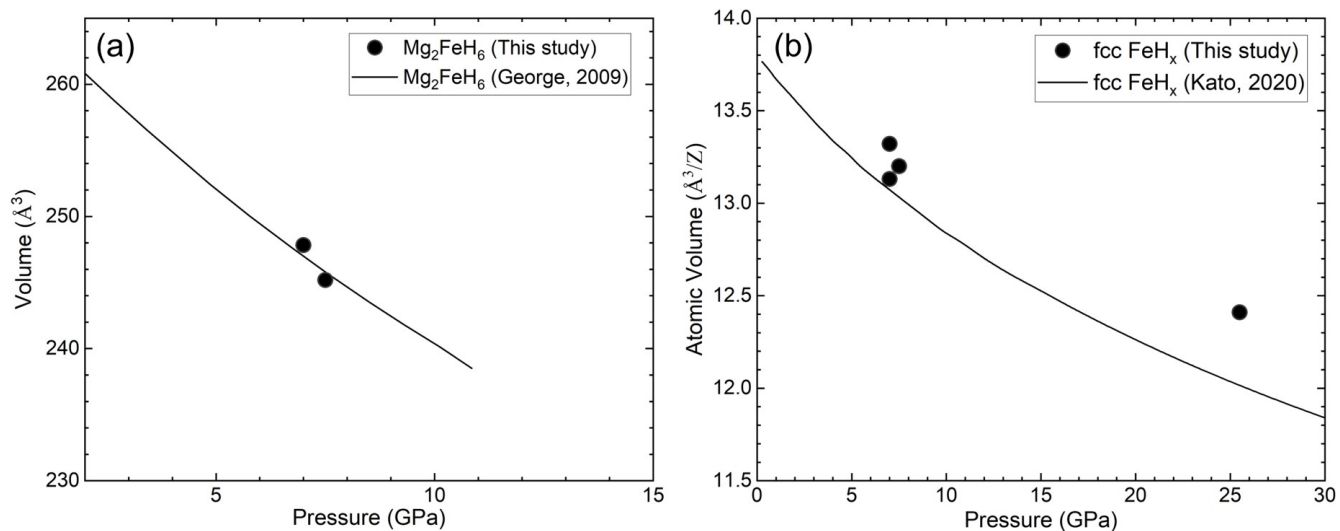


**Fig. S5.** (a) The unit-cell volumes of  $\text{Mg}_2\text{FeH}_6$  measured in this study compared with the equation of state from (38) at high pressures. (b) The atomic volume of fcc  $\text{FeH}_x$  measured in this study compared with the equation of state from (57) at high pressures. The volume of fcc  $\text{FeH}_x$  measured in this study is greater than the known values for  $x = 1$  (57). The estimated hydrogen content,  $x$ , is up to 1.2 based on the methods presented in (21).

DRAFT

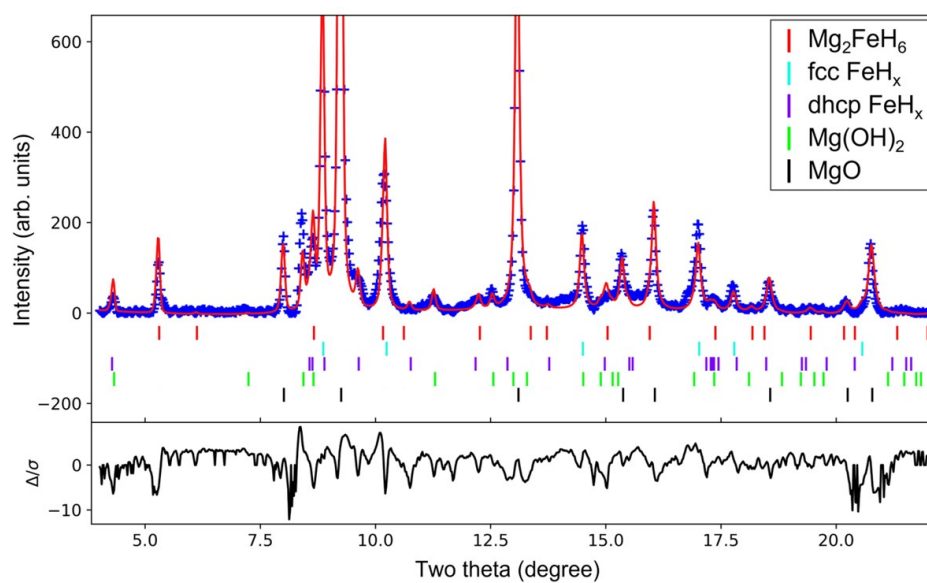


**Fig. S6.** The Le Bail analysis for the XRD pattern in Fig. 2a. The blue crosses are the measured intensities, and the red line is the calculated diffraction pattern after fitting. The black line at the bottom is the difference between the observed and the calculated diffraction patterns. The colored ticks indicate the diffraction positions of the identified phases. We used the  $Fm\bar{3}m$  (#225) space group for  $\text{Mg}_2\text{FeH}_6$  (40). The unit-cell parameters for the observed phases are:  $a = 6.268 \text{ \AA}$  for  $\text{Mg}_2\text{FeH}_6$ ,  $a = 3.747 \text{ \AA}$  for fcc  $\text{FeH}_x$ ,  $a = 2.562 \text{ \AA}$  and  $c = 8.834 \text{ \AA}$  for dhcp  $\text{FeH}_x$ ,  $a = 3.048 \text{ \AA}$  and  $c = 4.451 \text{ \AA}$  for  $\text{Mg}(\text{OH})_2$ , and  $a = 4.145 \text{ \AA}$  for  $\text{MgO}$ .



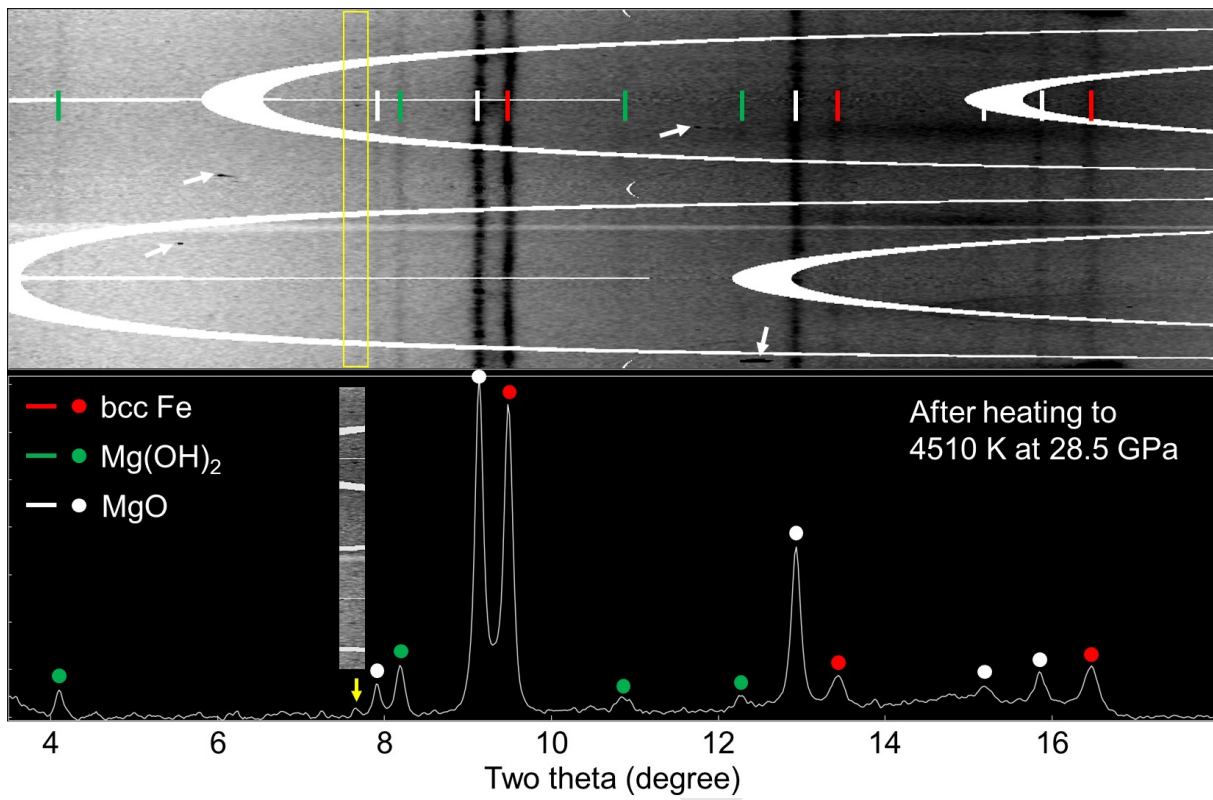


**Fig. S7.** X-ray diffraction data measured at 1 GPa after heating to 4510 K at 28.5 GPa (#26-016). The yellow box with the yellow arrow highlights an unidentified peak. The white arrows in the unrolled 2D image indicate defects in the detector.

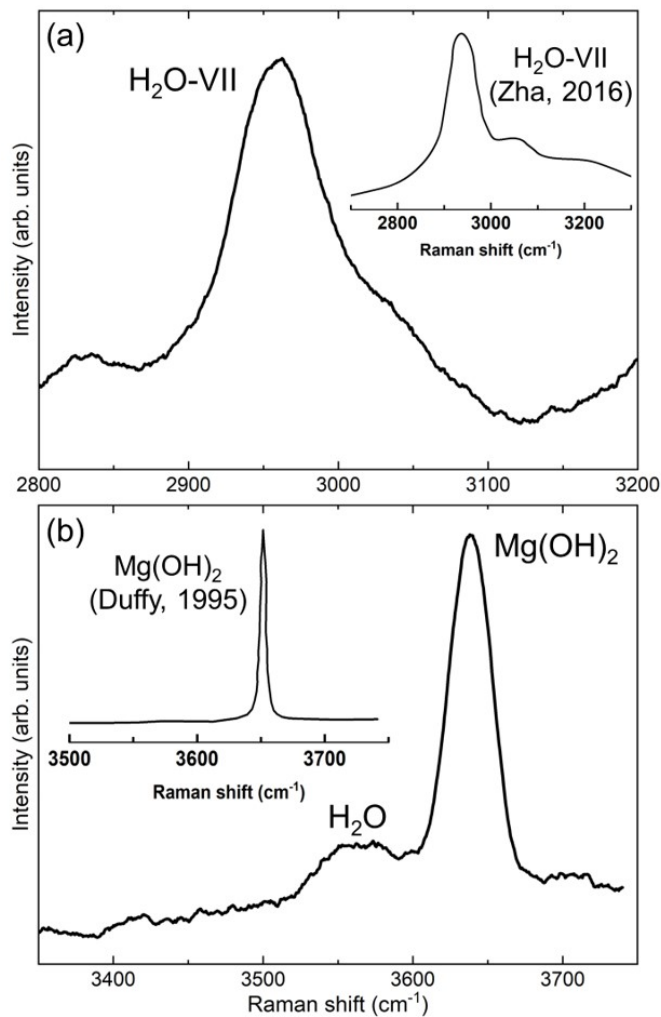


**Fig. S8.** Raman spectra measured at (a) 6.1 GPa and (b) 1.1 GPa during pressure decrease to 1 bar after heating experiments at 28.5 GPa and 4510 K, and 26 GPa and 4870 K, respectively (Table S1). Pressures were determined by the ruby fluorescence close to the gasket. The insets are for H<sub>2</sub>O-VII from (31) in (a) and Mg(OH)<sub>2</sub> from (30) in (b). In (b), a weak peak at  $\sim 3560\text{ cm}^{-1}$  can be assigned to H<sub>2</sub>O.

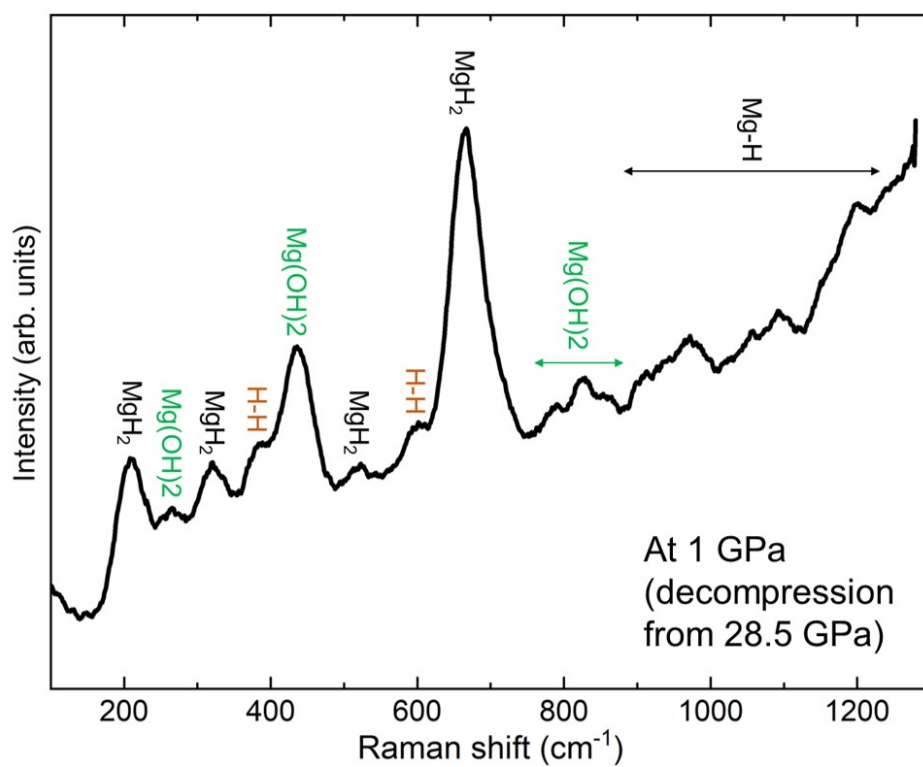


**Fig. S9.** Raman spectrum measured at  $\sim 1.0$  GPa for the sample heated at 28.5 GPa and 4510 K (#26-016). The spectrum in this figure and Fig. S10b are from different spots in the same heated area. The peak assignments were made by using previous reports on pure phases:  $\text{Mg}(\text{OH})_2$  (30),  $\text{H}_2$  (52),  $\gamma\text{-MgH}_2$  from (33) and the Mg–H stretching modes of  $\text{MgH}_2$  from (32).

DRAFT

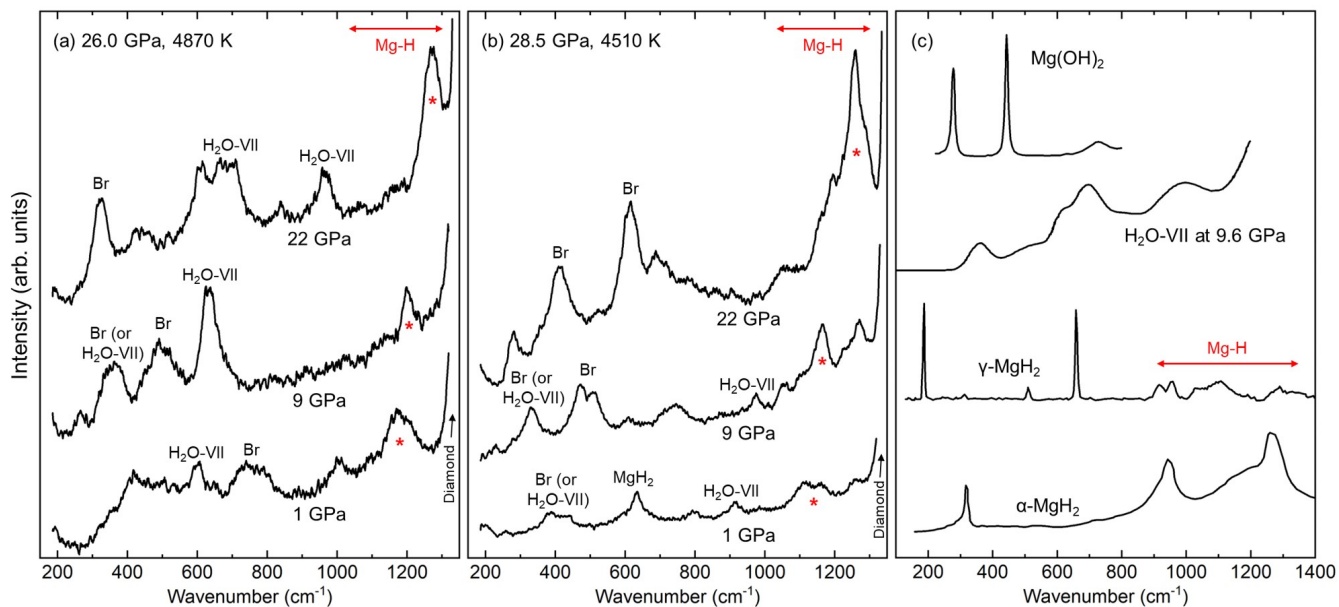


**Fig. S10.** Raman spectra measured after laser heating to (a) 4870 K at 26 GPa and (b) 4510 K at 28.5 GPa. (c) Raman spectra from previous studies reported for Mg(OH)<sub>2</sub> at 1 bar(30), H<sub>2</sub>O-VII at 9.6 GPa (31), α-MgH<sub>2</sub> at 1 bar, and γ-MgH<sub>2</sub> at 1 bar (33). In (a) and (b), Raman spectra were obtained at 22 GPa, 9 GPa, and 1 GPa for two different heated areas during decompression to 1 bar. The modes of Br (brucite; (30)), H<sub>2</sub>O-VII (Ice-VII; (31)), MgH<sub>2</sub> (α-MgH<sub>2</sub> and γ-MgH<sub>2</sub>; (33)) and Mg-H (the stretching modes of MgH<sub>2</sub>; (32)) were labeled in a and b. The red arrow denotes the range of the Mg–H stretching modes of MgH<sub>2</sub>. The Mg–H stretching vibrational modes exist between 1000 and 1300 cm<sup>-1</sup> (32, 33). The red stars highlight the peaks related to the Mg–H modes.

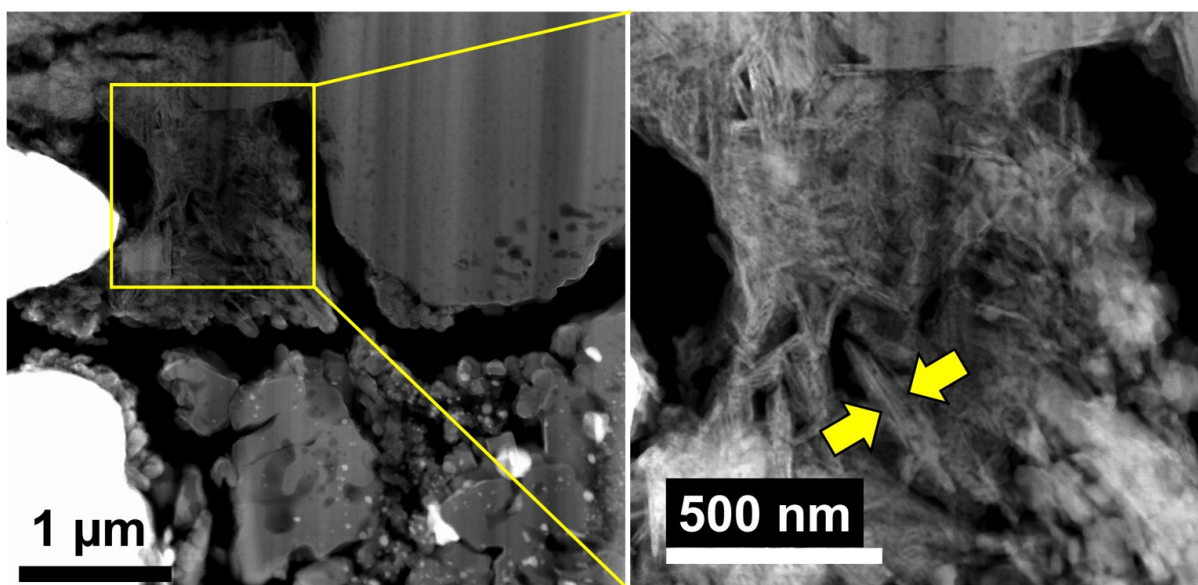


**Fig. S11.** Scanning-transmission electron microscopy (STEM) images of the sample recovered from run #31-003 (11.5 GPa and 3820 K). The zoomed-in area was shown on the right. At the edge of the heated area (the yellow box in the left image), elongated platy grains (indicated by the yellow arrows) are observed, and they are  $\text{Mg}(\text{OH})_2$ , as found in our XRD patterns. Similar structures were also reported for  $\text{Mg}(\text{OH})_2$  in (29).

DRAFT

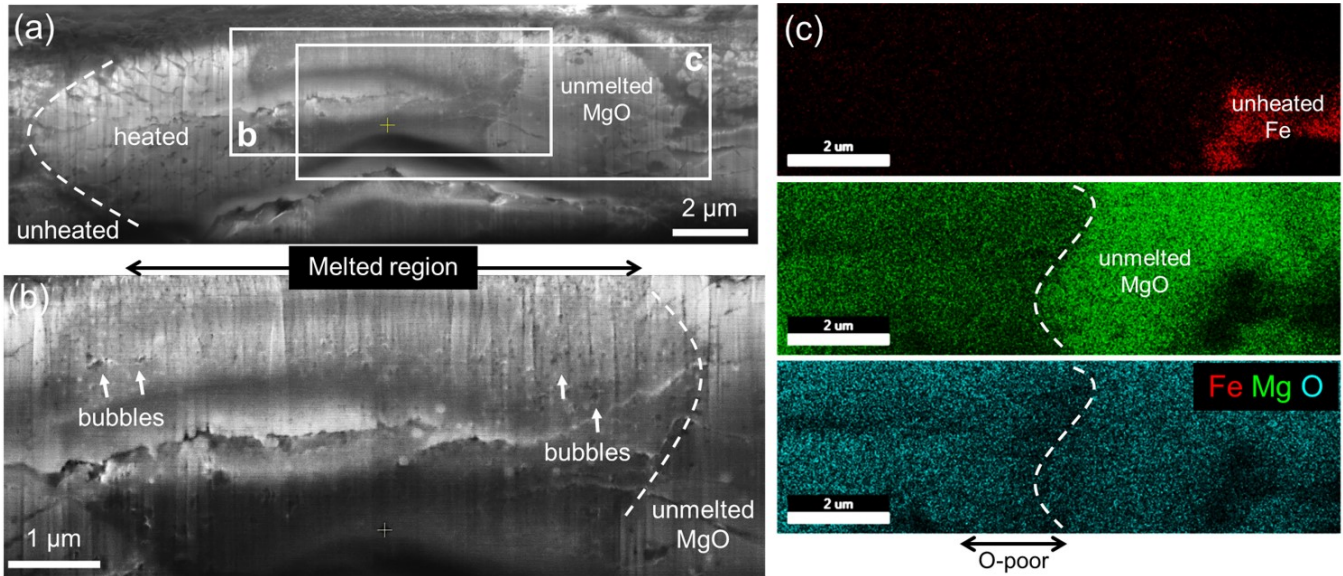


**Fig. S12.** Scanning electron microscopy (SEM) images (a and b) and EDS maps (c) of the heated area in the samples recovered from run #26-009 (26 GPa and 4870 K). The images here show the opposite side of the cross section presented in Fig. 4c. (a) The white dashed line divides the heated and the unheated areas. A relatively low voltage (10 kV) used for the imaging reveals the differences in texture between the heated area and the surrounding unheated areas. (b) The center of the heated area was melted. The melted region has many bubble-shaped structures. Some of them are highlighted by the white arrows. (c) Elemental maps for Fe, Mg, and O. The melted area has lower Mg than the unheated areas. The O-poor region matches with the region with the bubble-shaped structures. In this study, we observed that MgO is decomposed, and Mg and H become miscible at high temperatures (Eq. 2). The process produces Mg dissolved in H fluid and H<sub>2</sub>O. The melted region in b overlaps with the area with weak Mg and O signals in c. As explained in the main text, the bubble-shaped structure can be formed from H<sub>2</sub>O, H<sub>2</sub>, and Mg-H fluid exsolved during temperature quench at high pressure. These fluids in the bubble-shaped structures should have left when pressure was decompressed completely to 1 bar. Because of some materials would be removed in this way, this process can result in the weak Mg and O signals compared with the unheated regions with MgO on the sides.



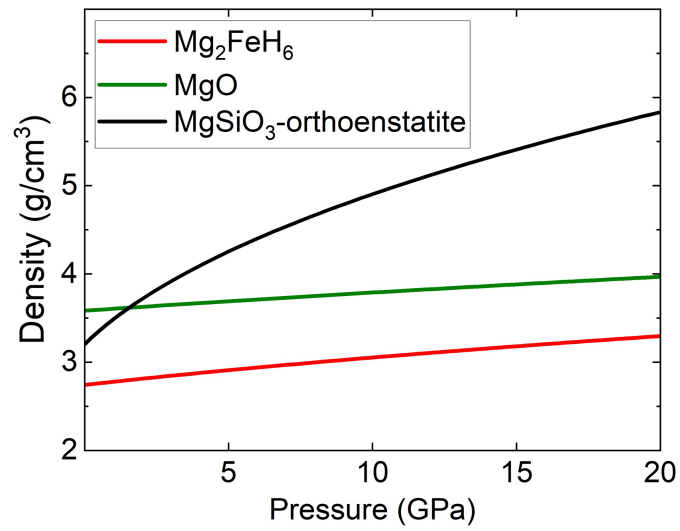


**Fig. S13.** The densities of Mg<sub>2</sub>FeH<sub>6</sub> (38), MgO (53), and MgSiO<sub>3</sub>-En (orthoenstatite) (42) calculated from their equations of state at high pressures and 300 K. Mg<sub>2</sub>FeH<sub>6</sub> is much less denser than planetary silicates and oxides.

DRAFT

**Table S1. Experimental runs in this study. \*O–H vibration mode was identified in Raman spectra. \*\*dhcp FeH<sub>x</sub> is likely metastably observed because the diffraction peaks are broader than those of other phases. Uncertainties for pressures and temperatures are 10% of the given value and 1 $\sigma$  (given in parentheses), respectively. XRD: X-ray diffraction, TEM: Transmission electron microscopy, SEM: scanning electron microscopy, fcc: face-centered cubic, dhcp: double hexagonal close-packed.**

Run #	<i>P</i> (GPa)	<i>T</i> (K)	Synthesized phases	Note
31-003	11.5	3820(420)	Mg <sub>2</sub> FeH <sub>6</sub> FeH <sub>x</sub> (fcc and dhcp**) Mg(OH) <sub>2</sub> H <sub>2</sub> O*	XRD (Fig. S3b) Raman (Fig. 3b) TEM (Figs 4a, 4b, and S11)
31-005	12.5	4770(650)	Mg <sub>2</sub> FeH <sub>6</sub> FeH <sub>x</sub> (fcc and dhcp**) Mg(OH) <sub>2</sub> H <sub>2</sub> O*	XRD (Figs 2a and S6) Raman (Fig. 3a) SEM (Fig. S2)
31-008	8.5	3500(300)	Mg <sub>2</sub> FeH <sub>6</sub> FeH <sub>x</sub> (fcc and dhcp**) Mg(OH) <sub>2</sub> H <sub>2</sub> O*	XRD (Fig. S4a) Raman
26-007	24.5	3570(300)	FeH <sub>x</sub> (fcc) Mg(OH) <sub>2</sub>	XRD (Fig. S4c)
26-009	26.0	4870(490)	FeH <sub>x</sub> (fcc) Mg(OH) <sub>2</sub> H <sub>2</sub> O*	XRD (Fig. S4b) Raman (Figs 3c, S8b, and S10a) SEM (Figs 4c, 4d, and S12)
26-012	28.0	3810(650)	FeH <sub>x</sub> (fcc) Mg(OH) <sub>2</sub> H <sub>2</sub> O*	XRD Raman
26-016	28.5	4510(270)	FeH <sub>x</sub> (fcc) Mg(OH) <sub>2</sub> H <sub>2</sub> O*	XRD (Fig. 2b) Raman (Figs S8a, S9, and S10b)

**Table S2.** The unit-cell volume of  $\text{Mg}_2\text{FeH}_6$  and the atomic volume of  $\text{FeH}_x$ . These data points are used in Fig. S5. Uncertainty for the volume is  $1\sigma$  given in parentheses. Uncertainty for pressure is smaller than 10% of the given value.  $Z$  is the number of formula units in the unit cell (for example,  $Z = 4$  for fcc  $\text{FeH}_x$ ).

Run #	$P$ (GPa)	$\text{Mg}_2\text{FeH}_6$ ( $\text{\AA}^3$ )	fcc $\text{FeH}_x$ ( $\text{\AA}^3/Z$ )
31-003q	7.0	247.82(72)	13.13(24)
31-005q	7.0	247.64(91)	13.32(34)
31-008q	7.5	245.19(98)	13.20(5)
26-016q	25.5	—	12.41(9)